The interaction of a Sears-type sinusoidal gust with a cambered aerofoil in the presence of non-uniform streamwise flow

Anna M. Young*
University of Bath, Bath, UK

Amanda S. M. Smyth†
University of Cambridge, Cambridge, UK

The unsteady load response of an aerofoil encountering a gust is often modelled using analytical transfer functions, which assume idealised behaviour of both the flow and the aerofoil. One such transfer function is the Sears function, which models a pure transverse gust interacting with a flat-plate aerofoil at zero mean incidence. The function was extended by Goldstein and Atassi to account for camber and incidence as well as the presence of a streamwise gust component. Atassi showed that the effects of camber and incidence (i.e. non-zero mean aerofoil loading) are not negligible when there is a streamwise gust component. In this work, new experimental data is shown for an aerofoil with non-zero loading encountering a gust with both streamwise and transverse components. The data gives validation of the Atassi model. Some of the flow physics behind the Atassi model is also investigated, including the superposition of the gust onto the aerofoil potential field and the propagation of the gust along the aerofoil surface.

Nomenclature

A_N, B_N	Fourier Coefficients	ζ	Wind tunnel correction factor
c	Aerofoil chord		***Accents and brackets***
C_P	$= \frac{P-P_{in}}{P_{0in}-P_{in}}$ Pressure coefficient	$\hat{}$	Amplitude
C_L	$= \frac{L}{\frac{1}{2}\rho U_\infty}$ Lift coefficient	$'$	Value when distorted by potential field
f	Frequency (Hz)	$\|\ \|$	modulus
k_1	Reduced frequency of transverse gust		***Subscripts***
k_2	Reduced frequency of streamwise gust	A	As modelled by Atassi
L	Lift (N)	AS	Atassi function normalised by Sears quasi-steady lift
m	Aerofoil camber (% chord)	corr	Corrected for wind tunnel height
P	Pressure	d	Distortion due to aerofoil
R	Unsteady lift normalised by Quasi-steady lift	flap	Pertaining to the flaps
S	Sears function	G	Gust
t	Time	GP	Predicted Gust
u	Streamwise velocity perturbation (m/s)	GM	Measured Gust
v	Transverse velocity perturbation (m/s)	QS	Quasi-steady
α	Angle of incidence	Sears	S
ϵ	Atassi gust magnitude	∞	Freestream quantity
ϕ	phase		
ρ	Density (kg/m^3)		

*Lecturer, Department of Mechanical Engineering, University of Bath, Claverton Down Road, BA2 7AY, UK.
†Research Associate, Whittle Laboratory, 1 JJ Thomson Ave, CB3 0DY, UK

I. Introduction

In many of the applications of fluid mechanics, it is necessary to know the unsteady load response of an aerofoil to a gust, but computing the response using a high-fidelity CFD code or undertaking detailed experimental analysis is often prohibitively expensive and time-consuming. For this reason, engineers often use analytical transfer functions, which assume idealised behaviour of both the flow and the aerofoil. One such transfer function is the Sears function[1], which assumes a pure transverse gust interacting with a flat-plate aerofoil with zero mean incidence. The Sears-type gust is shown in Fig. 1(a): a uniform streamwise flow of velocity U_∞ and a transverse sinusoidal gust of amplitude $\hat{v}$ and reduced frequency k_1 encounters a flat plate at zero mean incidence, giving rise to an unsteady incidence variation $\hat{\alpha}_G$.

An extension to the Sears function was derived by Goldstein and Atassi[2,3]. The Atassi function models the flowfield shown in Fig. 1(b), which has a transverse gust identical to the Sears gust, but an additional streamwise gust of magnitude $\hat{u}$ and reduced frequency k_2 is introduced. Further to this, the Atassi function models an aerofoil with both camber and incidence and thus takes into consideration the non-zero mean loading of the aerofoil and the arising potential field. Recent work by Wei et al.[4] studied an unloaded aerofoil in a gust with both transverse and streamwise components. They showed that the Atassi function gives good agreement with wind tunnel data, and they show that in the absence of aerofoil loading (as is the case for their un-cambered aerofoil at zero angle of attack), the difference between the Sears and Atassi functions is simply a matter of normalisation. This is because the second order terms in the Atassi function are only present when the mean aerofoil load is non-zero, as will be discussed in Section V.

Given the increased applicability of the Atassi function over the Sears function, it is perhaps surprising that little work has been undertaken on its validation and limitations. Furthermore, wind tunnel facilities that aim to generate a Sears-type gust will often use a series of flaps, or louvres. These flaps will either introduce a vertical variation in the flow due to the wakes from the flaps (if they are closely spaced) or allow deviation of the flow far from the flaps (if the flaps are spaced widely apart), and thus a smaller gust amplitude than expected. If a vertical variation is introduced to the flow, the gust will resemble the flow modelled by Atassi as opposed to that modelled by Sears. Wei et al.[4] showed the switch from Sears-type to Atassi-type flow by varying the flap spacing, while Jancauskas et al.[5] tested a gust generator with only two widely-spaced flaps and found generally good agreement with the Sears function.

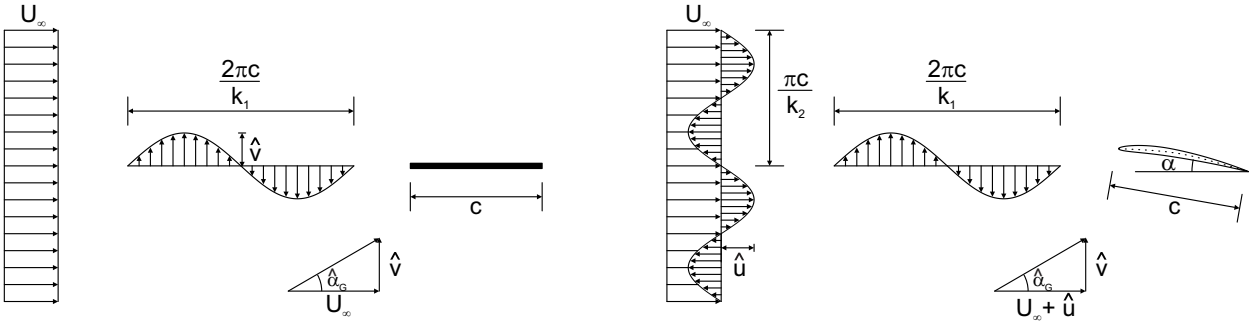

(a) Sears function.

(b) Atassi function.

Figure 1. Sketch of the aerofoil gust encounters modelled by the Sears and Atassi functions, including the definitions of k_1, k_2 and $\hat{\alpha}_G$ used in this work.

One of the applications in which the Sears function is used is the estimation of tidal turbine blade fatigue life. In this paper, therefore, an aerofoil representative of a tidal turbine blade is used for the experiments. This aerofoil is thicker (21% chord) than those typically used in aerodynamics experiments, and has significant camber (2% chord). Some data of this type was presented by Cordes et al.[6] with a cambered Clark-Y section at different angles of attack, but it was later stated by Traphan et al. and Wei et al. that the gust in their facility has a substantial component in the spanwise direction (i.e. the gust is three-dimensional)[7,4], and so the Atassi function would not be expected to apply.

The data shown in this paper therefore gives new information on the response of an aerofoil with camber and at non-zero angle of attack to an Atassi type gust; these are the conditions (when the aerofoil loading is non-zero) in which the Atassi function differs significantly from the Sears function and so these experiments provide new insights into the flow behaviour.

The paper is structured as follows. After an overview of the Sears and Atassi functions, the experimental

facility and method are described. The flowfield in the wind tunnel is examined under both steady and unsteady flow with and without the aerofoil with the aim of testing the assertion of Goldstein and Atassi that the incoming gust and the upstream aerofoil potential field will superpose linearly [2]. The unsteady lift measured in the experiments is then compared with the predictions of the Sears and Atassi functions, and the effects of both camber and incidence are examined. Some limits of agreement between the Atassi function and the experimental data are also found. Finally, a brief examination is undertaken of the propagation of the gust down each surface of the aerofoil, to see whether there is evidence of the gust being stretched on the suction surface due to the faster local flow.

II. Unsteady transfer functions: the Sears and Atassi functions

The Sears function [1] can be used to find the unsteady lift caused on an aerofoil by a sinusoidal transverse gust, as shown in Fig. 1(a). The function was derived assuming zero mean aerofoil loading (zero thickness, camber and mean angle of attack), but does not lose accuracy when applied to aerofoils with non-zero mean loading, if the gust is purely transverse (i.e. with no k_2 component) [2]. The Atassi function was developed by Goldstein and Atassi [2,3] to account for the distorting effect of the mean aerofoil potential field on the gust, for gusts with both transverse and streamwise components of velocity fluctuations. It is shown schematically in Fig. 1(b).

In order to obtain the unsteady lift amplitude, in each case a transfer function is multiplied by the quasi-steady lift, $\hat{L}_{\mathrm{QS}}$. The Sears function gives the unsteady lift as:

$$\hat{L}_{\mathrm{S}} = S(k_1)\hat{L}_{\mathrm{QS}} \tag{1}$$

where $S(k_1)$ is the Sears transfer function. The Atassi function gives the lift as a combination of the Sears transfer function and two additional terms:

$$\hat{L}_{\mathrm{A}} = \left[S(k_1)\frac{k_1}{|k|} + \alpha\hat{L}_{\alpha}\left(k_1, k_2\right) + m\hat{L}_{m}\left(k_1, k_2\right) \right] \hat{L}_{\mathrm{QS}} \tag{2}$$

The second and third terms in Equation 2 are both zero if k_2 is zero. The second term relates to the steady angle of attack, α, in radians, and the third to aerofoil camber, m,s as a fraction of the aerofoil chord length. The expressions $\hat{L}_{\alpha}\left(k_1, k_2\right)$ and $\hat{L}_{m}\left(k_1, k_2\right)$ are complicated functions of the gust frequencies, and can be found in the original work [2].

A recent study by Wei et al. [4] investigated the differences between Sears-style and Atassi-style gusts, and carried out experimental validation of both transfer functions for a thin symmetric aerofoil at zero mean angle of attack. This means that no aerofoil loading was included in the analysis, and any difference in load response between the Sears and Atassi gusts was due to the nature of the gust – whether or not it had a significant k_2 component. Wei et al provide valuable insight into the Atassi function, showing that one of the primary differences from the Sears function is its definition of quasi-steady lift, ($\hat{L}_{\mathrm{QS}}$). Both functions are normalised by the quasi-steady lift, and for the Sears function this is defined as:

$$\left(\hat{L}_{\mathrm{QS}}\right)_{\mathrm{S}} = 2\pi\rho c U_{\infty}\hat{v} \approx \pi\rho c U_{\mathrm{inf}}^2\hat{\alpha}_{\mathrm{g}} \tag{3}$$

where c is the aerofoil chord, and $\hat{\alpha}_{\mathrm{G}}$ is the amplitude of the inflow angle fluctuation generated by the gust. For the Atassi function, the quasi-steady lift is instead given by:

$$\left(\hat{L}_{\mathrm{QS}}\right)_{\mathrm{A}} = \pi\rho c U_{\infty}^2\epsilon \tag{4}$$

This time, the gust amplitude is defined by the parameter ϵ, which is a combination of the amplitude of both the streamwise and transverse gust fluctuations, from the following relations:

$$\hat{u} = \frac{U_{\infty}\epsilon k_2}{|k|} \tag{5}$$

$$\hat{v} = \frac{U_{\infty}\epsilon k_1}{|k|} \tag{6}$$

Wei et al showed that, given that the gusts have small amplitudes ($\hat{u} \ll U_\infty$, $\hat{v} \ll U_\infty$), the parameters ϵ and $\hat{\alpha}_{\mathrm{G}}$ can be related as follows:

$$\hat{\alpha}_{\mathrm{G}} = \tan^{-1}\left(\frac{\hat{v}}{U_\infty + \hat{u}}\right) \approx \tan^{-1}\left(\frac{\hat{v}}{U_\infty}\right) \approx \frac{\epsilon k_1}{|k|} \tag{7}$$

where

$$|k| = \sqrt{k_1^2 + k_2^2} \tag{8}$$

This relation means that the difference between the quasi-steady lift as defined in the Sears and Atassi functions lies in the factor $k_1/|k|$. Wei et al showed that for a symmetric aerofoil at zero mean angle of attack, the Atassi function was equivalent to the Sears function if multiplied by $|k|/k_1$, regardless of the value of k_2.

As explained by Atassi [3] and by Wei et al. [4], significant differences between the Sears and Atassi functions only emerge when there is *both* a k_2 component in the gust, *and* non-zero mean aerofoil loading due to camber or angle of attack.

An example of a case where the Atassi and Sears functions give significant differences in response is given in Fig. 2(a). This figure shows the response functions obtained from the Sears and Atassi functions, for an aerofoil with 2% camber and 3° mean angle of attack, undergoing oblique gust forcing ($k_1 = k_2$). The response function is defined as follows for the Sears function:

$$R_{\mathrm{S}} = \frac{\hat{L}_{\mathrm{S}}}{\left(\hat{L}_{\mathrm{QS}}\right)_{\mathrm{S}}} = S(k_1) \tag{9}$$

while for the Atassi function it is given by:

$$R_{\mathrm{A}} = \frac{\hat{L}_{\mathrm{A}}}{\left(\hat{L}_{\mathrm{QS}}\right)_{\mathrm{A}}} = S(k_1)\frac{k_1}{|k|} + \alpha \hat{L}_\alpha\left(k_1, k_2\right) + m\hat{L}_m\left(k_1, k_2\right) \tag{10}$$

In order to show a more direct comparison between the Sears and Atassi functions, a third response function is defined by multiplying the Atassi function by $|k|/k_1$, thus normalising it by the same quasi-steady lift as is used in the Sears function:

$$R_{\mathrm{AS}} = \frac{\hat{L}_{\mathrm{A}}}{\left(\hat{L}_{\mathrm{QS}}\right)_{\mathrm{S}}} \tag{11}$$

In order to illustrate the differing contributions of the incidence and camber effects, the functions $\hat{L}_\alpha\left(k_1, k_2\right)$ and $\hat{L}_m\left(k_1, k_2\right)$ are shown separately on Fig. 2 for the same aerofoil and gust conditions.

Unlike the work of Wei et al. [4], the experiments undertaken in this work use an aerofoil with camber at different angles of incidence. This will test the assertion that it is only in the presence of both a vertical (k_2) gust component and non-zero mean aerofoil loading that the results differ significantly from the Sears result.

III. Experimental Method

A schematic of the wind tunnel is shown in Fig. 3, and the key parameters of the tunnel are given in Table 1. The working section has solid side walls but is open at the top and bottom, to allow the flow to turn freely as it passes over the aerofoil. A 2D aerofoil is mounted at mid-height and two chords downstream of the tunnel inlet. The aerofoil profile was chosen to be representative of a tidal turbine aerofoil, and so has moderate camber (2% chord) and is relatively thick (21% chord). The aerofoil is mounted on a turntable in order to vary the angle of attack without moving the position of the leading edge in the tunnel. Circular fillets of radius 3% span were fitted at the junction between the aerofoil and the wind tunnel endwalls. These fillets were found to suppress the endwall corner separation and prevent it from affecting the flow over the majority of the aerofoil span, thus giving the desired 2D flow at mid-span.

Upstream of the working section there are a vertical series of flaps. The flap cross-section is a NACA-0012. The flaps are extruded Aluminium, and on both surfaces of each flap, there is a carbon-fibre stiffener

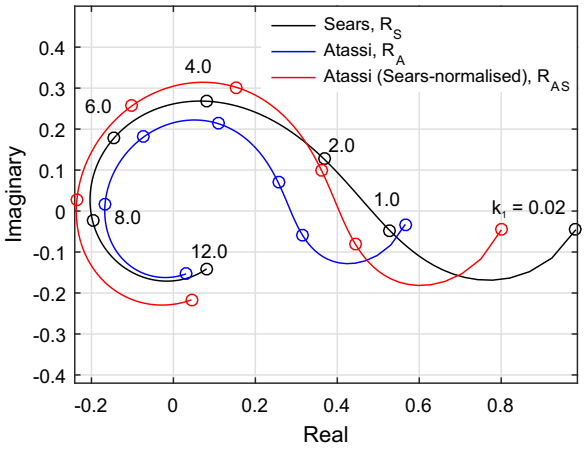

(a) Comparison of Sears and Atassi response functions.

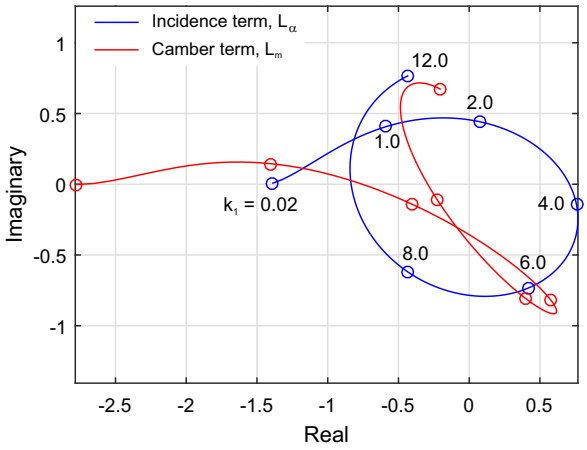

(b) Camber and incidence terms for the Atassi function.

Figure 2. Example Sears and Atassi response functions for an oblique gust ($k_1 = k_2$) interacting with an aerofoil with 2% camber at 3°aerofoil incidence.

Parameter	Value
Tunnel height (m)	1.00
Flow speed (m/s)	18.0 - 26.0
Aerofoil chord (m)	0.115
Aerofoil aspect ratio	2.96
Aerofoil Reynolds number	1.41 - 2.08x10^5
Number of flaps	58
Flap chord (mm)	35
Flap frequency range (Hz)	0 - 8
Reduced frequency range	0 - 0.35

Table 1. Key parameters of the wind tunnel

of thickness 0.5 mm. The stiffeners prevent spanwise bending of the flap and were not found to have an adverse effect on the flow quality downstream of the flaps. The flap chord was chosen as a balance between the need for stiffness (which sets a minimum thickness) and the desire to minimise unsteady flow behaviour of the flaps (the reduced frequency of the flap motion will be related to the reduced frequency of the gust encountered by the main aerofoil by $k_{\text{flap}} = c_{\text{flap}}/c_{\text{aerofoil}}$).

The decision of how many flaps to install was made by considering the behaviour of an infinite number of flaps with infinitesimal loading. In this case, the flaps would generate a continuous vortex sheet as envisaged by Sears. The flaps were therefore packed as tightly as possible which gave a ratio of 0.5 between the flap chord and the vertical spacing of the flaps. Placing the flaps further apart would also risk introducing flow deviation away from the flap surfaces.

The flaps are mounted in bearings on an Aluminium frame and attached to a DC motor via a cam and a connecting rod. The mechanism can therefore generate a sinusoidal variation in flow incidence similar to the Sears' type gust. The amplitude of the gust can be varied by changing the cam size, and the frequency is adjusted by changing the speed of the motor. For steady-state tests, the flaps are held in either their fully up or fully down position.

The tunnel operating conditions are measured using a sidewall static pressure tapping and a rake of Pitot probes between the flaps and the aerofoil, as shown on Fig. 3. The reference velocity from these probes is within 1% of the average inlet velocity integrated over the central portion of the wind tunnel. The incoming flow has a turbulence intensity of approximately 0.5%.

The aerofoil pressure distribution is measured using 43 aerofoil surface pressure tappings at midspan. The tappings are connected to fast-response pressure transducers via a set of semi-infinite lines. The use of semi-infinite lines enables high-frequency measurements to be taken in confined spaces by removing the requirement for the transducers to be mounted on the aerofoil surface[8]. The amplitude and phase of the

response does, however, change with frequency and so the tappings with semi-infinite lines were calibrated against a surface-mounted fast-response transducer using a signal generator and a loudspeaker. The resonant frequency of the tappings was found to be over 200 Hz, which is above the range of frequencies of interest in this work. For steady state tests, the tappings are connected to the transducers without the semi-infinite lines.

An unsteady total pressure probe was traversed vertically through the flow at various axial locations upstream of the aerofoil (see Fig. 3 for the positions). By measuring the flow three times with the probe oriented at three angles (-45°, 0°, +45°) the equivalent data from a fast-response three-hole probe could be reconstructed and thus the flow angle and speed could be calculated. This enabled the gust to be characterised in space and time both with and without the aerofoil installed.

Data were sampled at 20 kHz for 20-30 seconds depending on the frequency of the flaps. All data were phase-locked to the motor frequency using a once-per-revolution sensor on the shaft. This enabled the harmonic response to be averaged over 50-150 cycles.

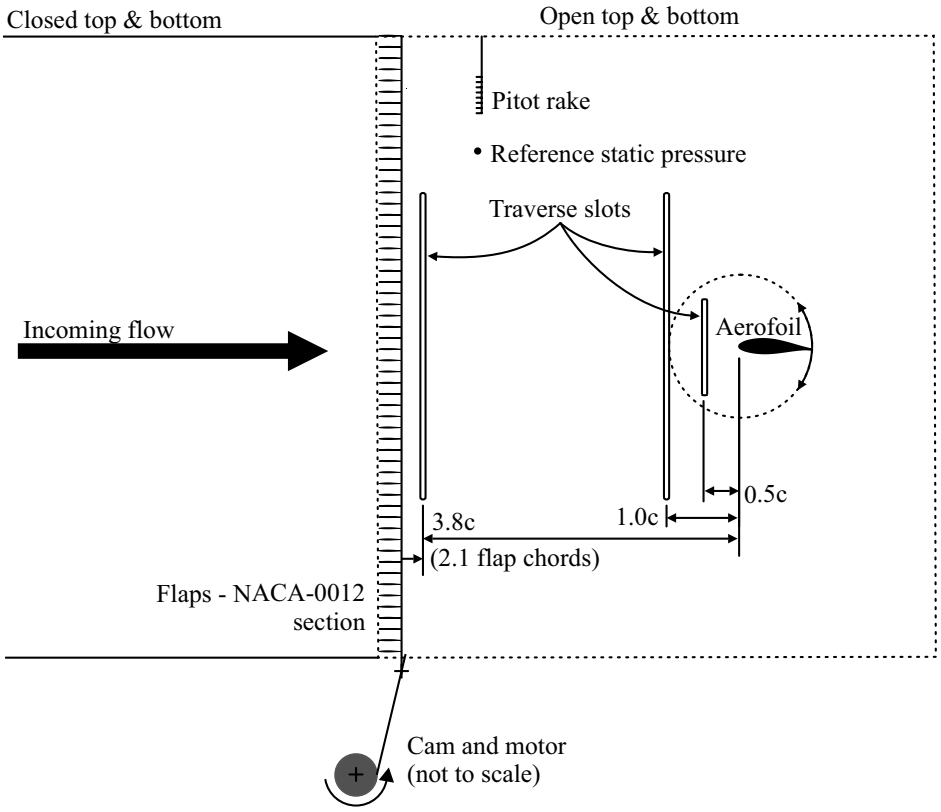

Figure 3. Schematic of the wind tunnel test facility showing traverse plane locations.

IV. Steady-state behaviour of the aerofoil

The wind tunnel generates a finite jet with a height of approximately 8 times the aerofoil chord. This means that the aerofoil will behave slightly differently to an aerofoil in an ideal, infinite flow, as explained by Brooks et al.[9, 10, 11]. The most obvious consequence of the finite jet is that the lift is lower than expected and thus the lift curve does not follow the ideal $2\pi\alpha$ rule. This can be rectified by dividing the apparent angle of attack by a correction factor ζ. Correlations for ζ were developed for a zero-camber aerofoil by Brooks et. al[9, 10]. For the aerofoil used in this work, the correction factor was found to be 1.19, which agrees with their correlation. In tests with a larger aerofoil (which will be discussed briefly in Section V), however, the correlation was found 5% higher than the value given by Brooks et al. This may be due to the fact that the aerofoil used in this work has non-negligible camber and thickness.

Steady-state tests were undertaken with the flaps in both the 'up' and 'down' positions, such that the

true incidence was:

$$\alpha_{\text{corr}} = \frac{(\alpha - \alpha_{\text{flap}})}{\zeta} \tag{12}$$

A graph of lift coefficient against incidence corrected using Equation 12 with the flaps in two positions is shown in Fig. 4(a). The data from the wind tunnel is compared with results from MSES (a coupled Euler-boundary layer solver[12]). It can be seen that both the flaps up (blue) and flaps down (red) data follow the same line with gradient 2π as the MSES prediction (black line) at angles below the stall angle. The stalling behaviour of the aerofoil differs between MSES and the experiments; this is due to the large blockage generated when the aerofoil is at angles far from zero and the presence of aerofoil-endwall corner separations at high incidence. From this point onwards, all incidence values given for experimental data have been corrected using Equation 12.

The reason for the reduction in lift in a finite jet is explained by Brooks et al.[9] as being due to the restriction of the aerofoil potential field: there is a condition of zero velocity potential at the jet boundary and so the aerofoil can be considered to be in an infinite cascade. The correction found above will only match the total aerofoil lift - the surface pressure distribution will still be different in the finite jet case, and the potential field around the aerofoil will not match. It is possible to develop an aerofoil with an adjusted camber line which will produce the pressure distribution of the wind tunnel test when operating in an infinite jet. Brooks et al. give an analytical solution for this 'free equivalent foil' which is valid for zero-camber, thin aerofoils[9].

For the aerofoil considered here, the error in pressure distribution is quite small. This is shown in Fig 4(b), where the measured surface pressure (dots) is compared with data from MSES (solid lines) at three different incidences. It can be seen that there is good agreement between the simulations and the experiments. This is may be due to fact that the jet height ratio of 8 used in this work is towards the upper end of those used in the literature (Brooks et al.[11] undertook tests with jet ratios from 0.5 to 11).

The aerofoil potential field will distort an incoming gust, and this may affect the resulting unsteady load. In the case of a Sears-type gust, the potential field and the gust will behave independently, but Atassi[3] argues that the presence of vertical non-uniformities in the gust will cause coupling between the gust and the potential field. Goldstein and Atassi[2] state that the incoming gust and potential field will superpose linearly, but that the gust convection speed will be different across the two surfaces of the aerofoil (in contrast to the frozen gust hypothesis, which is valid for an un-loaded aerofoil). This difference in convection speed is what causes the discrepancy between coupled and uncoupled gust response. These points will be discussed in the next three sections.

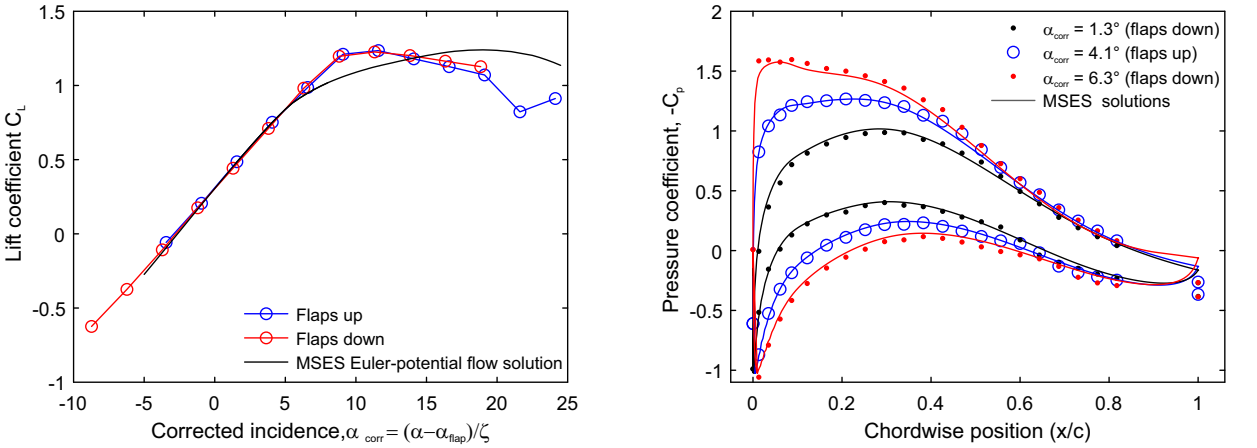

(a) Lift coefficient against corrected incidence.

(b) Surface pressure distributions with the aerofoil at three different incidences.

Figure 4. Lift curve and surface pressure distributions from MSES and experimental data showing good agreement when the wind tunnel correction factor is applied to the incidence.

V. Unsteady gusts and their interaction with the aerofoil potential field

The flow angle variation due to the aerofoil potential field is shown in Fig 5(a), which is taken from an MSES simulation in infinite flow at zero angle of attack. As expected, the most substantial changes in flow

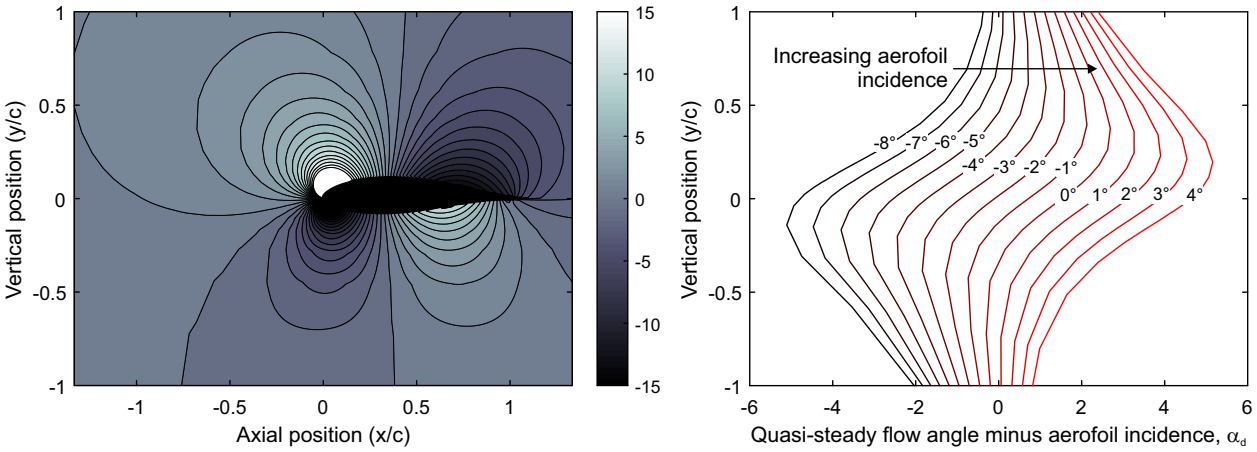

(a) Flow angles round the aerofoil at zero incidence.

(b) Distortion angle against vertical postion at x/c = -0.5.

Figure 5. Data from MSES simulations showing the effect of the aerofoil potential field on the incoming flow angle.

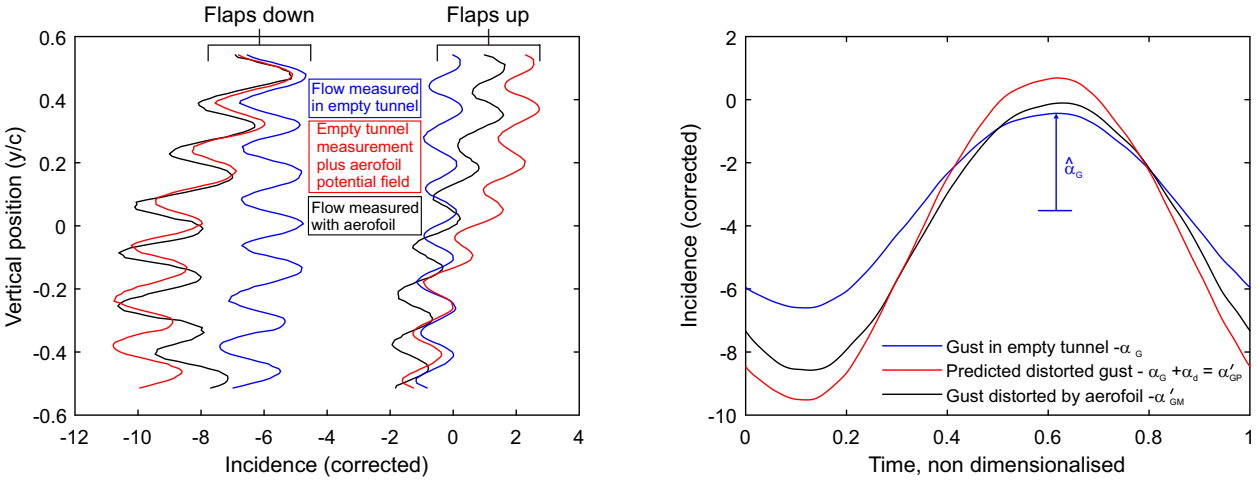

(a) incidence against vertical position for steady-state flow with the flaps in two positions.

(b) Incidence against time for a gust with reduced frequency k = 0.13.

Figure 6. Traverses at x/c = -0.5 with the flaps in the up and down position showing the effect of the aerofoil on the steady-state flow compared with the no-aerofoil case with the predicted potential field from MSES.

angle are close to the aerofoil, but the aerofoil also exerts a non-negligible influence on the upstream flow. To see this more clearly, the change in flow angle relative to the mean incidence is shown in Fig. 5(b); this distortion is defined as α_d. The data is taken from 0.5 chords upstream of the aerofoil and from simulations at incidences from -8° (black) to +4° (red). Distortions of up to 4° from the mean incidence are observed, with the flow being deflected up on the top surface of the aerofoil and down on the bottom surface. The distortion in the flowfield is not linear with average incidence or with vertical position, and the maximum distortion increases with aerofoil loading.

The flow angle measured in the wind tunnel with the aerofoil in place will be affected by this distortion. If the assertion of Goldstein and Atassi[2] is correct, then the measured distorted gust, α'_{GM}, will be the sum of the gust measured in the empty wind tunnel α_G and the distortion due to the quasi-steady aerofoil potential field, α_d. The quasi-steady distortion, α_d, can be found from the data shown in Fig. 5(b), by interpolating for the measured empty-tunnel incidence (this interpolation is done after the wind tunnel correction factor, ζ, has been applied to the empty tunnel data). We denote this predicted gust incidence as α'_{GP}:

$$\alpha'_{GP} = \alpha_G + \alpha_d \tag{13}$$

In Fig. 6, the incidence variation measured 0.5 chords upstream of the aerofoil with the aerofoil in place, α'_{GM}, (black) is compared with the empty wind tunnel measurements, α_G, (blue) and the predicted distorted gust, α'_{GP}, as defined in Equation 13 (red).

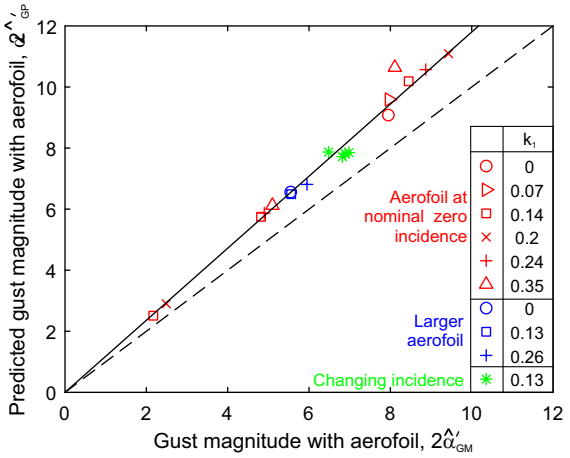

(a) Predicted gust magnitude against measured gust magnitude with aerofoil.

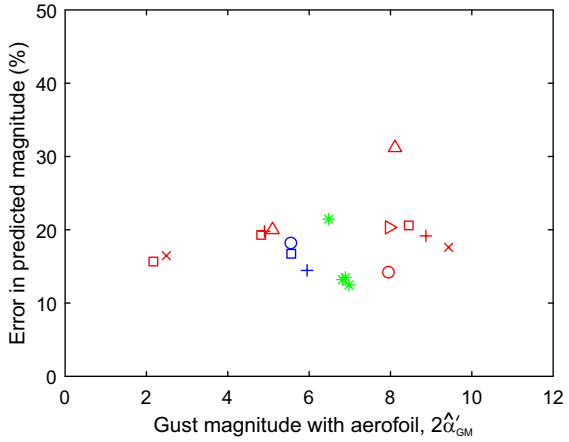

(b) Error in predicted gust magnitude against measured gust magnitude with aerofoil.

Figure 7. Measured flow angles at x/c = -0.5 with and without the aerofoil in place, compared with the angles obtained by adding the no-aerofoil data to the simulated aerofoil potential field from Fig. 5(b).

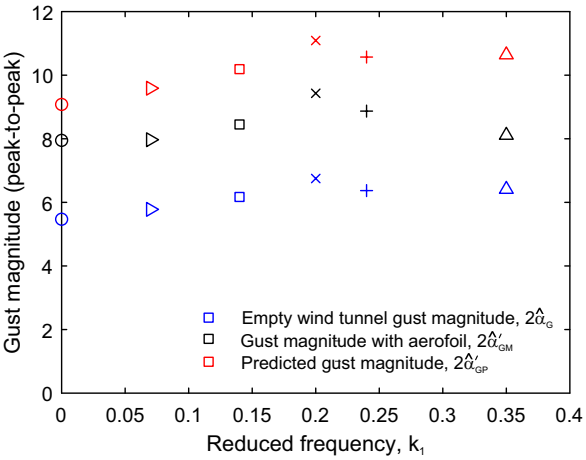

(a) Gust magnitude against reduced frequency, k_1.

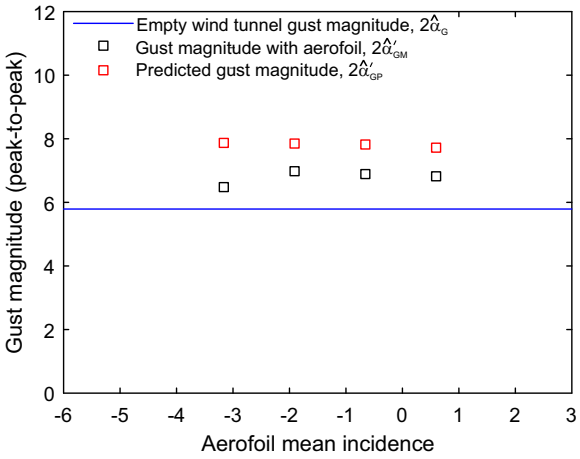

(b) Gust magnitude against aerofoil mean incidence.

Figure 8. Effect of reduced frequency and aerofoil mean incidence on the magnitude of the gust in the empty wind tunnel and with the aerofoil in place (both predicted and measured).

Fig. 6(a) shows the flow angles with flaps stationary in two different positions. Considering first the empty wind tunnel data (blue), it can be seen that with the flaps in the 'up' position, the flow angle is approximately -0.4°, while the angle reduces to -5.8° when the flaps are moved to the 'down' position. In both cases, the wakes from the flaps are visible, causing a 1-2° variation in flow angle, but other than this the flow angle is approximately constant across the traverse range. When the aerofoil is in the wind tunnel, the measured angle, α'_{GM}, is indeed different from α_G. As expected from Fig. 5, the effect of the aerofoil potential field is different at the two mean incidences shown in Fig. 6(a): in the flap up case, the incidence is increased at positions above the aerofoil and reduced slightly below the aerofoil, while the flap down case shows a large reduction in incidence below the aerofoil, reducing to nothing at the top of the measurement plane.

The trend in the predicted flow, α'_{GP} (shown in red), is approximately correct, but the magnitude of the distortion is over-predicted. This is particularly apparent in the data from the top half of the traverse plane with the flaps up, where the distortion predicted by MSES, α_d (the difference between the blue and red lines), is approximately twice the size of the measured distortion (the difference between the blue and black lines). When averaged over the traverse plane, α'_{GP} for the flaps up case is 1.0° higher than the measured angle, α'_{GM}, while the difference in the flaps down cases is 0.2° (this smaller value is within the experimental error bounds). This discrepancy between the distortion predicted by MSES and the measured data suggests that the aerofoil potential field is, indeed, affected by the boundaries of the finite jet, despite the agreement of the surface pressure distributions with MSES (Fig. 4(b)).

The effect of finite jet height on the upstream potential field has not been studied in much detail, perhaps due to the historically greater difficulty in measuring the flowfield as opposed to the aerofoil forces and pressure distribution. A CFD study was conducted by Moreau et al.[13], in which they compared the potential field of an aerofoil in an infinite jet with those obtained with finite height to chord ratios of 1.0 and 3.8. Their results show qualitatively that the incoming flow behaves differently as the jet height changes but they do not suggest any means of correcting for this effect.

When the flaps are moving, a similar gust distortion is observed to that discussed above, i.e. the gust is larger when the aerofoil is installed than in the empty wind tunnel case. An example of this is shown in Fig. 6(b), which shows the gusts generated by the flaps at a reduced frequency, k_1, of 0.13. The data is taken from the same traverse plane as Fig. 6(a) and the incidence has been averaged over the whole vertical range at each time-step.

It can be seen that the flaps generate a sinusoidal incidence variation in time when the wind tunnel is empty (blue line, α_{G}). This blue line gives the Sears gust amplitude $\hat{\alpha}_{\mathrm{G}}$, as marked on the plot. With the aerofoil in place at a nominal incidence of 0° (black line)[a], the gust is distorted such that the minimum incidence is reduced by approximately 2° while the maximum incidence increases by under 0.5°. The gust also deviates from a perfect sinusoid, with a slight skewing of the peak to a later time than that in the empty tunnel case. The predicted distorted gust, α'_{GP} (Eq. 13) is shown in red. Both the increase in gust magnitude and the skewing of the peak are predicted by this superposition. As in the steady case, however, the amplitude of the gust is over-predicted relative to the measured data.

Gusts of three different amplitudes were generated at a variety of reduced frequencies from 0 (steady) to 0.35, and the gust was measured with and without the aerofoil in place at its nominal zero incidence as in Fig. 6(b). The peak-to-peak amplitude of the predicted distorted gust ($2\hat{\alpha}'_{\mathrm{GP}}$) is plotted against the actual gust amplitude measured with the aerofoil in place ($2\hat{\alpha}'_{\mathrm{GM}}$) in Fig. 7(a). The data points from this set of tests are shown in red, with different markers denoting each reduced frequency. The dotted black line denotes exact agreement between the measured and predicted gusts ($\hat{\alpha}'_{\mathrm{GP}} = \hat{\alpha}'_{\mathrm{GM}}$), while the solid black line shows a straight line through the red points which has equation $\hat{\alpha}'_{\mathrm{GP}} = 1.18\hat{\alpha}'_{\mathrm{GM}}$. The error between the predicted and measured gust size is shown in Fig. 7(b), where it can be seen that it is between 10 and 20% for all but one case. This data therefore shows that the error between the gust distortion predicted by MSES and that measured in the wind tunnel is independent of gust size or frequency, and that adding the correct quasi-steady field to the unsteady gusts would give a distorted gust very close to the actual distorted gust. These results suggest that the superposition of the two flowfields is linear and is not affected by unsteady coupling over the frequency range tested.

The effect of reduced frequency on the amplitude of the gust both with and without the aerofoil is shown more clearly in Fig. 8(a), which is a plot of incidence change against reduced frequency for the cases with the largest cam (which gives a peak-to-peak incidence variation of just under 6° in the empty wind tunnel case - Fig. 6). Considering first the blue markers, which show the data from the empty wind tunnel, there appears to be a slight increase in gust amplitude with reduced frequency, but the change is within the range of the experimental error and there is significant scatter in the results. The actual gust amplitude (black markers) follows the same trend as the empty tunnel results: the steady-state and $k_1 = 0.35$ results are almost equal. When the empty gust data is superposed with the potential field from MSES, the data represented by the red markers are obtained. The slight upward trend in the no-tunnel data is exaggerated by the superposition process, but the error is approximately constant with reduced frequency.

The average error of 18% is very close to the wind tunnel incidence correction factor discussed in Section IV, which is 1.19. This adjustment has, however, already been taken into consideration in the calculations shown in Fig. 7(a). Also shown on Fig. 7(a) are three measurements taken with a larger aerofoil of 230 mm chord (blue)[b]. The wind tunnel correction factor for this aerofoil is 1.51, but the data lies on the same line as that from the smaller aerofoil, with an average error of 18%.

If the aerofoil incidence is changed, the quasi-steady potential field will change, as shown in Fig. 5(b). The effect of this on the superposition of the gust with the potential field was investigated by measuring the gust with the aerofoil at four different angles. The results of this are shown in Fig. 8(b), which is a plot of peak-to-peak amplitude change against aerofoil incidence for the gust with a reduced frequency, k_1 of 0.13 shown in Fig. 6(b). Restrictions in the traverse slot arrangement meant that the flowfield had to be measured further upstream of the aerofoil (1.0 chords instead of 0.5 chords), and so the overall distortion is lower than

[a]This corresponds to a corrected mean incidence of -3.2°, using Equation 12

[b]This data is taken from 0.5 chords upstream of the larger aerofoil, i.e. twice as far away in absolute terms.

in the other cases. Nevertheless, the same trend is observed - the blue line shows the magnitude of the gust in the empty wind tunnel, while the black squares show the gust with the aerofoil in place at each incidence. There is very little change in the distortion of the gust by the aerofoil across the incidence range tested, despite the lift coefficient changing by approximately 0.4 over this range. As with all the previous data, the prediction from superposing the quasi-steady potential field with the empty-tunnel gust (red squares) gives a larger amplitude than the actual data.

The data from the cases with varying aerofoil incidence is denoted by the green stars on Figs 7(a) and (b). It can be seen that the error is consistent with all the other cases, suggesting that aerofoil incidence does not affect the superposition of the gust with the potential field (at least for attached flow). Taken as a whole, this data shows that the gust and the aerofoil potential field superpose linearly regardless of gust reduced frequency, aerofoil chord and angle of attack. The reason for the consistent error between $\hat{\alpha}'_{\mathrm{GP}}$ (the prediction obtained by addition of the simulated quasi-steady field to gust measured in the empty wind tunnel) and $2\hat{\alpha}'_{\mathrm{GM}}$, (the gust measured with the aerofoil in place) is unclear, but the fact that the error is unaffected by the magnitude of the aerofoil potential field or by the reduced frequency shows that there is no non-linear coupling of the two flowfields upstream of the aerofoil over the range of variables tested here.

The finding that the gust distortion is independent of reduced frequency is in line with the theory of Goldstein and Atassi[2], who state that the incoming gust will not have its amplitude changed by the steady-state flowfield. Goldstein and Atassi do state, however, that the wavelength of the gust will change over the aerofoil chord, and this will be discussed briefly in Section VII. Now that the gusts generated have been quantified, the aerofoil lift response can be compared with that predicted by the models of Sears and Atassi. This will be done in the next section.

VI. Aerofoil lift response

VI.A. Measuring unsteady lift

The unsteady component of lift was found by direct integration of the Fourier coefficients, A_{N} and B_{N}, for each surface pressure measurement at the gust frequency, f_{gust}:

$$A_{\mathrm{N}} = \frac{2}{M}\int_0^M P(t)\sin\left(2\pi f_{\mathrm{gust}}t\right)dt; \tag{14}$$

$$B_{\mathrm{N}} = \frac{2}{M}\int_0^M P(t)\cos\left(2\pi f_{\mathrm{gust}}t\right)dt; \tag{15}$$

where $P(t)$ is the pressure signal and M is the length of the sample (which was set to be many gust cycles, see Section III). The two Fourier coefficients combine to give the phase and amplitude of the response at each location (once a calibration has been applied to take into account the phase lag and attenuation due to the semi-infinite lines). The unsteady pressure difference is then integrated along the aerofoil chord to give the lift. This measured value of unsteady lift can then be compared with the load predicted by the Sears and Atassi functions.

VI.B. Calculating k_2 and ϵ

The frequency k_2 of the streamwise gust component has a significant impact on the result of evaluating the Atassi function. This means that it is vital to obtain an accurate estimate of k_2 when comparing experimental results with the Atassi function. An estimate of the spatial frequency in the vertical plane can be obtained from Figure 6(a) and the definition of k_2 given in Fig. 1(b). By this process, k_2 was estimated as approximately 20. Further investigation, however, suggests that this is not an appropriate way of measuring k_2. Instead, the approach of Wei et al.[4] should be taken and k_2 and ϵ must be calculated from the measured values of k_1 and $\hat{\alpha}_{\mathrm{G}}$ via a two-parameter fit to Equation 7. The results of this two-parameter fit for are shown in Fig. 9.

Figure 9(a) shows the relationship between the gust amplitude parameter, ϵ and measured gust amplitude $\hat{\alpha}_{\mathrm{G}}$. It can be seen that ϵ increases linearly with $\hat{\alpha}_{\mathrm{G}}$, as would be expected. Figure 9(b) shows the calculated k_2 values (blue stars), against measured gust amplitude, $\hat{\alpha}_{\mathrm{G}}$. The measured ranges of k_1 are included in

red for comparison. It can be seen that k_2 is relatively constant with increasing gust amplitude, and that it has a mean value of 0.035. The two-parameter fit method therefore gives a significantly lower value of k_2 than that which was calculated from the visual estimate of k_2 from Fig. 6(a) (which gave $k_2 = 20$). In the following sections it will be shown that this lower value of k_2 gives far closer agreement between the Atassi function and experimental data.

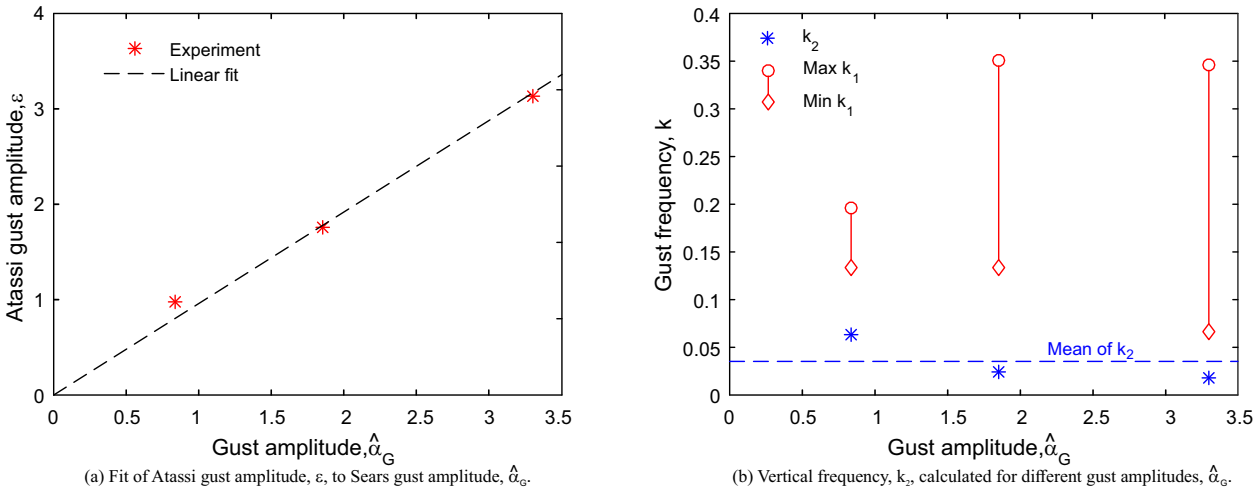

(a) Fit of Atassi gust amplitude, ε, to Sears gust amplitude, $\hat{\alpha}_G$.

(b) Vertical frequency, k_2, calculated for different gust amplitudes, $\hat{\alpha}_G$.

Figure 9. Results of the two-parameter fit for ϵ and k_2 from measured values of $\hat{\alpha}_G$ and k_1.

VI.C. Comparing analytical theory and experiments

Figure 10 shows the amplitude of the unsteady lift against k_1, calculated from the unsteady transfer functions and measured in experiments. Figure 10(a) shows the load amplitude normalised by the quasi-steady lift as defined by Sears (Eq. 3), while Fig. 10(b) uses the quasi-steady lift defined for the Atassi function (Eq. 4). The data is taken from tests at -0.7° mean angle of attack, which was the closest to zero of the available data range. The Atassi function is evaluated for the same aerofoil parameters, with k_2=0.035. Fig. 10(a) shows that in these conditions the Sears and Atassi functions are nearly identical when normalised consistently, and only diverge at low reduced frequencies (k_1 <0.1).

The experimental results in Fig. 10 have been categorised by gust amplitude, and the data from the intermediate gust amplitude (black dots, $\hat{\alpha}_G = 2°$) shows reasonable agreement with the transfer functions. The data from largest gust amplitude (red dots $\hat{\alpha}_G = 3°$) consistently shows lift amplitudes much lower than that predicted by Sears and Atassi, while the data from the smallest gust (blue dots $\hat{\alpha}_G = 2°$) is consistently higher than the model predictions. Looking at Fig. 10(b), the shape of the data for all three gust amplitudes matches the trend in the Atassi function, even in cases where the magnitudes are incorrect.

The quasi-steady lift, by which the unsteady loading is non-dimensionalised, is dependent on the measured gust amplitude. The estimated error in the gust amplitude measurements is ±0.25°, which is a substantial proportion of the overall gust amplitude. This is especially the case for the smallest amplitude gust, and changing the magnitude of the gust by 0.2° would bring the data into agreement with the analytical functions. The trends shown in the data in Figs 10 to 12 will not be affected by this error, only the absolute values on the y-axis, as all the data for a given gust size is non-dimensionalised by the same quasi-steady value.

Both transfer functions were developed for small amplitude perturbations, and as such are expected to lose accuracy in cases where the gust amplitude is large. It may be that the largest gust amplitude ($\hat{\alpha}_G = 3°$, i.e. a peak to peak amplitude of 6°), causes second-order viscous effects that cannot be captured by the unsteady transfer functions.

An exception to the agreement between the transfer functions and the experimental data for the gust amplitude $\hat{\alpha}_G = 2°$ can be seen in Figs 10(a) and (b), marked by hollow dots. These data points were all acquired during the same test run, and so it is likely that there was an error in the experimental method or post-processing during these tests. This set of data will, therefore, not be discussed further in this paper.

The mean angle of attack ($\alpha = -0.7°$) for the results in Fig. 10 was chosen such that the distorting effects of the aerofoil potential field were minimised, and the Sears and Atassi functions were similar in shape as possible, as in the work of Wei et al.[4]. Below, in Figs 11 and 12, the lift amplitude is shown against the

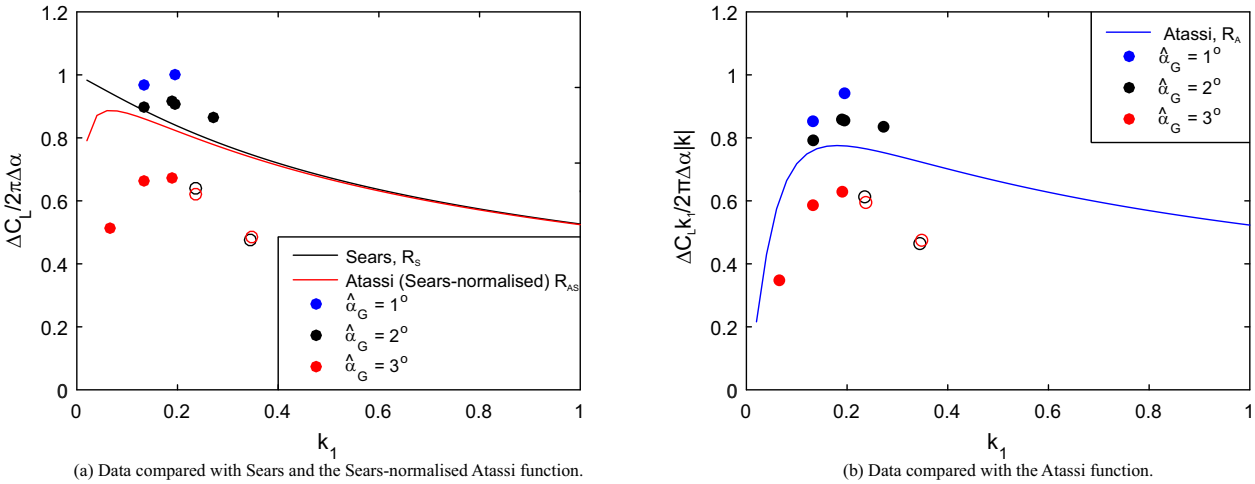

(a) Data compared with Sears and the Sears-normalised Atassi function.

(b) Data compared with the Atassi function.

Figure 10. Comparison of experimental data with the Sears and Atassi transfer functions with the aerofoil at a mean incidence of -0.7° across a range of gust amplitudes, $\hat{\alpha}_G$, and reduced frequencies, k_1.

changing mean angle of attack (α), in order to illustrate the effect of changing the aerofoil potential field on the results. In these figures the lift amplitude has been normalised by $\left(\hat{L}_{QS}\right)_{Sears}$.

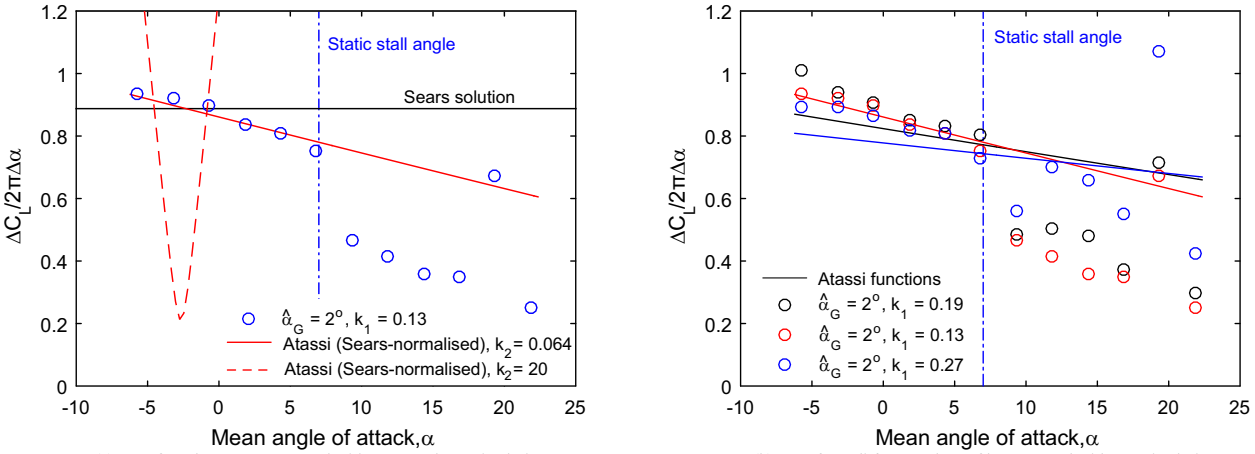

(a) Data from k $_1$= 0.13 compared with Sears and Atassi solutions.

(b) Data from different values of k$_1$ compared with Atassi solutions.

Figure 11. Amplitude of unsteady response against angle of attack, normalised by quasi-steady response as defined by Sears compared with the Sears and Atassi functions ($\hat{\alpha}_G = 2°$).

Figure 11 shows the results for experimental gust amplitude $\hat{\alpha}_G = 2°$. Figure 11(a) shows the results from a single experimental run (blue circles), and compares the data with both the Sears (black line) and Atassi (red line) functions. It can be seen that there is a marked reduction in the unsteady load response as the angle of attack increases. The Sears function does not model the effect of angle of attack and therefore the solution is constant across the range of tests given here. This means that the Sears solution disagrees with the experimental data when the angle of attack is not negligible. The Sears and Atassi solutions cross near the angle at which the aerofoil produces zero lift, as this is the point at which the effect of the aerofoil potential field switches sign.

The vertical dash-dot line indicates the static stall angle of the aerofoil (see Fig. 4(a)). Below this angle, the agreement between the experiment and the Atassi function is good. After this the agreement deteriorates, as is expected when the viscous effects of a stalled aerofoil impact the results. As an illustration, the Atassi function is also shown evaluated with k_2=20 (red dashed line), which was the original visual estimate of k_2 from Fig. 6(a). With the higher value of k_2, the Atassi function gives a much more dramatic variation in lift with changing α, indicating that the value of k_2 calculated from the two-parameter fit (Fig 9(b)) is the appropriate one to use, rather than the visual estimate.

Figure 11(b) shows the data in Fig. 11(a) (red circles) along with measurements from tests at two higher

values of k_1. The Atassi function evaluated at the respective values of k_1 is shown as a solid line. Again, the agreement is good up to the static stall angle of the aerofoil, though there is some disagreement in magnitude at the lowest angles of attack.

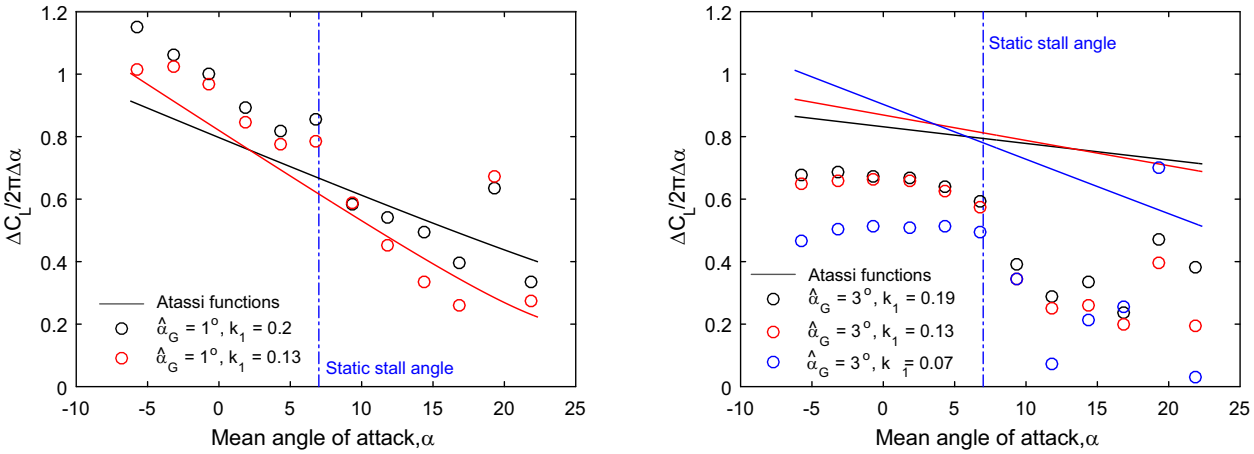

(a) Gust amplitude, $\hat{\alpha}_G$=2°. (b) Gust amplitude,$\hat{\alpha}_G$=3.5°.

Figure 12. The amplitude of the unsteady response, normalised by the quasi-steady response as defined for the Sears function, for increasing mean angle of attack, compared with the Atassi function with two different gust amplitudes.

In Fig. 10, it can be seen that the agreement between the data and the Atassi function is less good for the other gust amplitudes ($\hat{\alpha}_G = 1°$ and 3°). This is shown in more detail in Fig. 12, which shows plots of unsteady load amplitude against angle of attack with gust amplitudes, $\hat{\alpha}_G$, of 1° (Fig. 12(a)) and 3° (Fig. 12(b)). In Fig. 12(a), the gradient of the unsteady lift response follows the Atassi function, although the magnitude of the response is slightly under-predicted by the Atassi function. Again, a small error in the gust amplitude would account for this difference in magnitude. Beyond the static stall angle the agreement with Atassi deteriorates, as in the cases shown in Fig. 11.

Figure 12(b) shows the normalised lift against mean angle of attack for the largest gust amplitude ($\hat{\alpha}_G = 3°$). As mentioned above, this relatively large gust amplitude is likely to cause deviation between the Atassi function and the experimental results. In all the cases in Fig. 12(b), the experimental results give 50-70% of the unsteady lift amplitude predicted by Atassi, and the gradients are not well-predicted. Beyond the static stall angle the unsteady effects are dramatic, and some very large lift amplitudes suggest the presence of dynamic stall (which is also seen in Fig 12(a), and in Fig. 11).

VII. Speed of gust propagation along the aerofoil

As discussed in Section V, the potential flow upstream of the aerofoil has been shown to superpose linearly onto the gust, in line with the work of Goldstein and Atassi[2]. Goldstein and Atassi, however, predict that aerofoil loading *will* cause a difference in the propagation of the gust along the two surfaces, i.e. it will propagate faster along the suction surface where the velocities are higher than the freestream velocity, while it will move more slowly along the pressure surface. In this section we present some preliminary analysis suggesting that this is, indeed, the case.

From the Fourier analysis described in Section VI, the phase of the pressure fluctuations at each point on the aerofoil surface can be calculated:

$$\phi = \tan^{-1}\left(\frac{A_N}{B_N}\right) \tag{16}$$

The phases calculated in this way are plotted against axial position for four selected cases in Fig. 13. It should be noted that the pressure moves in opposite directions on the two surfaces (i.e. an increase in incidence causes a reduction in the pressure on the suction surface and an increase on the pressure surface), so if the two surfaces were responding 'in phase' with one another there would be an offset of π radians in their calculated phase. In order to aid comparison, the pressure surface data has been shifted by π radians.

The data is all phase-locked to the cam once-per-revolution signal, and the offset at the leading edge is somewhat arbitrary, as it is made up of a combination of the convection time of the gust from the flaps to the aerofoil and the phase lag of the aerofoil response.

Figure 13(a) shows the phase lag of the response at two different reduced frequencies. In both cases, the gust amplitude, $\hat{\alpha}_G$, is 2° and the aerofoil incidence is 3°. The measurements from the pressure surface are shown as blue circles while those from the suction surface are shown in red. There is substantial scatter in the data over the rear portion of the aerofoil; this is because the response is very small towards the aerofoil trailing edge and so the measurement accuracy is low. For each case shown, a straight line fit has been applied to the data from between the leading edge and $x/c = 0.34$, and a dash-dot line shows the path of the gust if it were to convect at the free-stream velocity, which is given by:

$$\Delta\phi_{\text{frozen}} = 2\pi\frac{T_{\text{gust}}}{T_{\text{conv}}} = 2\pi\frac{c}{U_\infty}\frac{k_1 U_\infty}{2\pi c} = k_1 \tag{17}$$

where T_{gust} is the gust timeperiod and T_{conv} is the time taken for the freestream flow to pass over the aerofoil.

It can be seen that in all cases there is a difference between the two aerofoil surfaces, with the suction surface points (red) showing increasing phase lag over the surface of the aerofoil, while those on the pressure surface show no change or a slight reduction in phase lag. When the reduced frequency is increased (top set of lines in Fig. 13(a)) the difference in phase between the two surfaces increases. This is likely to be due to the increase in the phase lag of a frozen gust along the aerofoil (Eq. 17).

Figure 13(b) shows the effect of aerofoil incidence on the phase change across the surfaces. The blue and red circles denote the phase on the pressure and suction surfaces, respectively, from a test with the aerofoil at -0.7° incidence, while the cyan and green squares are from a test with the aerofoil at 6.8° incidence. In these cases, the reduced frequency was fixed at 0.19 and $\hat{\alpha}_G$ was 1°. Again, the frozen gust phase is denoted by the dash-dot line. As in the previous cases, the phase lag increases with axial distance along the suction surface, while it stays constant or reduces slightly on the pressure surface. A difference can also be observed between the two cases - the higher incidence case shows a larger increase in phase lag on the suction surface, and possibly a smaller one on the pressure surface. This change between the two incidences can be attributed to the increase in loading with increased mean incidence and the accompanying increase in speed changes across the aerofoil surfaces.

Intuitively, it seems that the suction surface should exhibit a phase lead over the pressure surface, i.e. the opposite of what has been shown here. More work is therefore required to understand this data fully, but the preliminary analysis suggests that there is a difference in the way in which the gust convects along each aerofoil surface. This finding is in line with the argument of Goldstein and Atassi [2], and suggests that their model therefore is capturing the major effect of the aerofoil potential field on the unsteady load response.

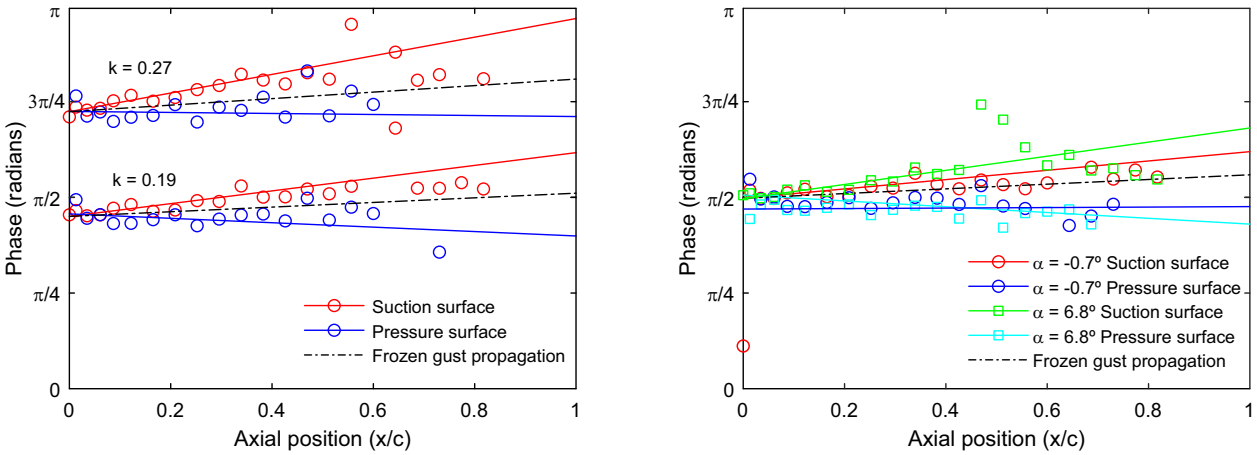

(a) Effect of reduced frequency with α= 1.8° and $\hat{\alpha}_G$ = 2°.

(b) Effect of aerofoil incidence with k_1 = 0.19 and $\hat{\alpha}_G$ = 1°.

Figure 13. Axial variation in phase of the response calculated from aerofoil surface pressure signals.

VIII. Conclusion

This paper has presented an examination of the unsteady load generated by an Atassi-type gust on an aerofoil with non-zero mean load. The results presented above suggest that the Atassi function can predict the effect of changes in mean aerofoil loading on the unsteady lift experienced by aerofoils, for transverse gusts with a streamwise oscillating component. In cases with small-to-moderate gust amplitude, the trends in unsteady response are replicated accurately in terms of the effects of both reduced frequency and aerofoil angle of attack. The agreement is good when the mean angle of attack is smaller than the static stall angle of the aerofoil; at higher angle of attack the lift response is more erratic and the agreement deteriorates.

With very small gust amplitudes, the experimental error in measuring the gust generates substantial uncertainty in the quasi-steady response, and so the absolute magnitude of the data may not be reliable. With very large gust amplitudes, the trends in the data are also not replicated by the Atassi function, suggesting that the second-order viscous effects have become significant.

One limitation of the Atassi function is that aerofoil thickness is not accounted for, although Goldstein and Atassi suggest that the effect of thickness may be of the same order of magnitude as that of camber and incidence angle[2]. The aerofoil used in the experiments above is chosen to represent the aerofoil section of a tidal turbine blade, which are generally thicker than those of for example wind turbines or aircraft. As such, discrepancies between the Atassi function and experiments could be caused by thickness effects.

Examination of the flowfield upstream of the aerofoil has shown that the gust and the aerofoil potential field can be considered to superpose linearly, i.e. there is no unsteady coupling of the incoming gust with the potential field. This was shown by comparing gust measurements with the aerofoil in place with the gust obtained by adding the quasi-steady potential field to the gust measured in the empty wind tunnel. This finding is in line with the analysis of Goldstein and Atassi[2].

A preliminary analysis was undertaken of the propagation of the gust along each surface of the aerofoil. Again, this data agrees with the statement of Goldstein and Atassi that the gust propagates at a different rate on the pressure and suction surfaces of the aerofoil due to the differing local flow velocities.

Overall, this paper shows first-of-a-kind validation of the Atassi function for an aerofoil with non-zero mean load encountering a gust with both streamwise and transverse components. Furthermore, the results presented here suggest that gust generation through the use of many small vanes generates gusts with very low k_2 values, despite the visual image of the flow field suggesting otherwise. Because of this, the lift amplitude was a relatively weak function of the mean angle of attack and camber, compared to what it would be at higher k_2. As future work, the flapping vanes will be fitted with serrated trailing edges, for the purpose of encouraging wake mixing and thus reducing k_2 even further and generating unsteady flow that is closer to a pure Sears-type gust.

Acknowledgements

The experiments described in this paper were funded by EPSRC grant EP/J010308/1. The authors wish to thank the technical staff of the Whittle Laboratory for their assistance in manufacturing the gust generator and test section - in particular, Mr David Barlow, Mr Ian Thornton and Mr Elliot Read. The authors would also like to thank Dr Ivor Day, Prof. Robert Miller, Dr Carl Sequeira and Mr Chris Freeman for the useful discussions during the course of this work.

References

[1] von Kármán, T., "Airfoil theory for non-uniform motion," *Journal of the Aeronautical Sciences*, Vol. 5, No. 10, 1938, pp. 379–390.

[2] Goldstein, M. E. and Atassi, H., "A complete second-order theory for the unsteady flow about an airfoil due to a periodic gust," *Journal of Fluid Mechanics*, Vol. 74, No. 4, 1976, pp. 741–765.

[3] Atassi, H., "The Sears problem for a lifting airfoil revisited-new results," *Journal of Fluid Mechanics*, Vol. 141, 1984, pp. 109–122.

[4] Wei, N. J., Kissing, J., Wester, T. T., Wegt, S., Schiffmann, K., Jakirlic, S., Hölling, M., Peinke, J., and

Tropea, C., "Insights into the periodic gust response of airfoils," *Journal of Fluid Mechanics*, Vol. 876, 2019, pp. 237–263.

[5] Jancauskas, E. and Melbourne, W., "The aerodynamic admittance of two-dimensional rectangular section cylinders in smooth flow," *Journal of Wind Engineering and Industrial Aerodynamics*, Vol. 23, 1986, pp. 395 – 408, Special Issue 6th Colloquium on Industrial Aerodynamics Building Aerodynamics.

[6] Cordes, U., Kampers, G., Meißner, T., Tropea, C., Peinke, J., and Hölling, M., "Note on the limitations of the Theodorsen and Sears functions," *Journal of Fluid Mechanics*, Vol. 811, 2017.

[7] Traphan, D., Wester, T., Peinke, J., and Guelker, G., "On the aerodynamic behavior of an airfoil under tailored turbulent inflow conditions," *5th International Conference on Experimental Fluid Mechanics ICEFM 2018 Munich*, 07 2018.

[8] Englund, D. and Richards, W. B., "The infinite line pressure probe," *NASA Technical Memorandum*, Vol. 24, 02 1985.

[9] Brooks, T., Marcolini, M., and Pope, D., "Airfoil trailing edge flow measurements and comparison with theory, incorporating open wind tunnel corrections," *9th Aeroacoustics Conference*, 1984, pp. 2266.

[10] Brooks, T. F., Marcolini, M. A., and Pope, D. S., "Airfoil trailing-edge flow measurements," *AIAA journal*, Vol. 24, No. 8, 1986, pp. 1245–1251.

[11] Brooks, T. F., Pope, D. S., and Marcolini, M. A., "Airfoil self-noise and prediction," *NASA Reference Publication 1218*, 1989.

[12] Drela, M., *A user's guide to MSES 3.00*, MIT, 2004.

[13] Moreau, S., Henner, M., Iaccarino, G., Wang, M., and Roger, M., "Analysis of flow conditions in freejet experiments for studying airfoil self-noise," *AIAA journal*, Vol. 41, No. 10, 2003, pp. 1895–1905.